







Ultrafast imaging of spontaneous symmetry breaking in a photoionized molecular system

Min Li ^{1,8}, Ming Zhang^{2,3,8}, Oriol Vendrell ⁴, Zhenning Guo², Qianru Zhu⁵, Xiang Gao⁵, Lushuai Cao⁵, Keyu Guo¹, Qin-Qin Su¹, Wei Cao ¹✉, Siqiang Luo¹, Jiaqing Yan¹, Yueming Zhou¹, Yunquan Liu ²✉, Zheng Li ²✉ & Peixiang Lu ^{1,6,7}✉

The Jahn-Teller effect is an essential mechanism of spontaneous symmetry breaking in molecular and solid state systems, and has far-reaching consequences in many fields. Up to now, to directly image the onset of Jahn-Teller symmetry breaking remains unreached. Here we employ ultrafast ion-coincidence Coulomb explosion imaging with sub-10 fs resolution and unambiguously image the ultrafast dynamics of Jahn-Teller deformations of CH_4^+ cation in symmetry space. It is unraveled that the Jahn-Teller deformation from C_{3v} to C_{2v} geometries takes a characteristic time of 20 ± 7 fs for this system. Classical and quantum molecular dynamics simulations agree well with the measurement, and reveal dynamics for the build-up of the C_{2v} structure involving complex revival process of multiple vibrational pathways of the CH_4^+ cation.

¹Wuhan National Laboratory for Optoelectronics and School of Physics, Huazhong University of Science and Technology, Wuhan, China. ²State Key Laboratory for Mesoscopic Physics and Collaborative Innovation Center of Quantum Matter, School of Physics, Peking University, Beijing, China. ³University of Science and Technology Beijing, Beijing, China. ⁴Physikalisch-Chemisches Institut, Universität Heidelberg, Heidelberg, Germany. ⁵MOE Key Laboratory of Fundamental Physical Quantities Measurement and Hubei Key Laboratory of Gravitation and Quantum Physics, PGMF and School of Physics, Huazhong University of Science and Technology, Wuhan, China. ⁶Hubei Key Laboratory of Optical Information and Pattern Recognition, Wuhan Institute of Technology, Wuhan, China. ⁷CAS Center for Excellence in Ultra-intense Laser Science, Shanghai, China. ⁸These authors contributed equally: Min Li, Ming Zhang. ✉email: weicao@hust.edu.cn; yunquan.liu@pku.edu.cn; zheng.li@pku.edu.cn; lupeixiang@hust.edu.cn

In the 1930s, Jahn and Teller discovered a now celebrated theorem demonstrating the intrinsic geometric instability of degenerate electronic states based on group theory¹. This instability leads to spontaneous symmetry breaking of the molecular structure, known as Jahn–Teller (JT) effect, which removes the degeneracy of the electronic state and lowers the overall energy of the molecules. Essentially, the JT effect originates from the coupling of electronic and nuclear degrees of freedom in molecules, and heralds the breakdown of the Born–Oppenheimer approximation², which is the basis for much of our understanding of molecular structure and dynamics. The JT effect is a widespread phenomenon occurring in a broad range of molecules, transition-metal complexes, and solids. From the fundamental physics perspective, the JT effect is a concrete example of spontaneous symmetry breaking, which has far-reaching consequences in quantum field theory and the Standard Model of particle physics, such as the Higgs mechanism³.

Structural properties appearing as a consequence of the JT effect have been extensively demonstrated in static measurements with high-resolution optical spectroscopy^{4–6}, electron paramagnetic resonance spectroscopy^{7,8}, rotationally resolved pulsed-field-ionization zero-kinetic-energy photoelectron spectra^{9–15}, as well as Coulomb explosion experiments^{16,17}. However, accessing the short-time structural dynamics caused by the JT effect, i.e., the onset of symmetry breaking from an initially symmetric configuration, remains a great challenge, and a direct experimental imaging of structural symmetry breaking in real time has not yet been realized, even in the ultrafast diffraction imaging experiment of excited CF_3I molecule, the JT distortion has not been resolved from the measured data due to insufficient resolution². Accessing these structural dynamics is key to understanding the early stages of photo-triggered chemical bond cleavage and molecular dynamics (MD) leading to energy and charge transfer processes¹⁸. In this connection, recent ground-breaking transient absorption spectroscopy measurements in crystals¹⁹ and molecules²⁰ report time-dependent energy level shifts immediately after the interaction with a pump pulse, which can be traced back to the onset of JT distortions. However a comprehensive, real-space picture of these ultrafast processes is still missing.

In this work, we propose and demonstrate a scheme to experimentally image the dynamics of the JT distortion and apply it to the photoionized methane cation. The methane cation is one of the simplest floppy systems exhibiting JT distortions in its triply degenerate ground state. The topology of the corresponding potential energy surfaces is well known²¹ and constitutes the basis for our analysis. A schematic of the dynamics unfolding after a strong pump laser pulse is illustrated in Fig. 1. The molecular geometry can be detected by Coulomb explosion imaging under the influence of a subsequent probe laser pulse. The strong pump laser pulse photoionizes CH_4 and populates the CH_4^+ in its ground 2F_2 state with T_d symmetry, which subsequently deforms owing to the JT effect. As the CH_4^+ cation reaches C_{3v} configuration, it experiences further JT symmetry breaking because the degeneracy of the 2E electronic state is not completely lifted. The cation will finally settle in C_{2v} configuration as the kinetic energy of the system is equilibrated. By simultaneously recording the kinetic energies and momenta of the fragments from two- and three-body Coulomb explosion as a function of the pump-probe time delay, the dynamics of the JT distortion is mapped in time and symmetry space.

Results

The measured kinetic energy release (KER) distributions are plotted in Fig. 2 as a function of the time delay between the two 25 fs pulses for the two-body breakup channels of $\text{CH}_3^+ + \text{H}^+$ and $\text{CH}_2^+ + \text{H}_2^+$. In order to separate Coulomb explosion events

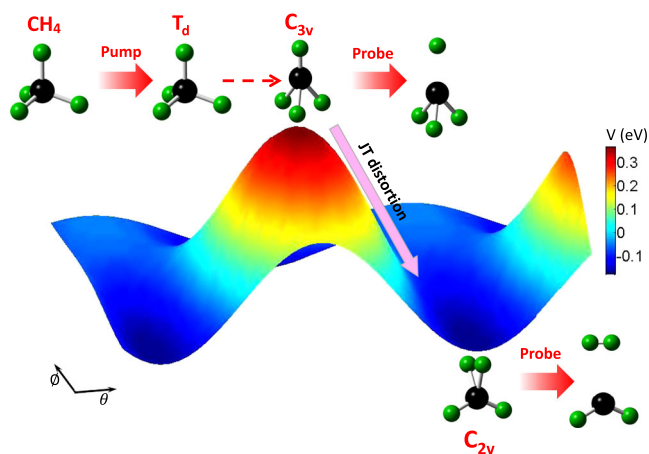


Fig. 1 Scheme of probing JT deformation in a photoionized CH_4^+ cation.

The CH_4^+ cation in a C_{3v} geometry (at the peak of the potential energy surface) undergoes JT distortion to a C_{2v} geometry (at the bottom of the potential energy surface) and the identified structural evolution pathway is indicated by the arrows. By recording the coincident fragments from Coulomb explosion of those geometries as a function of time between the pump-probe laser pulses, the dynamics of the JT deformation can be revealed.

from other dissociative fragmentation channels, only those events are shown where two ions have been detected in coincidence and fulfill the momentum conservation condition. One can see that the time-integrated KER is nearly the same for those two breakup channels. Both of them reveal the maximal yield at ~ 5 eV.

Zero time delay in Fig. 2 means that the pump and probe pulses come at the same time. One sees that the KER spectra are dominated by time-independent features at KER ~ 5 eV caused by the interaction with only one of the laser pulses²² (e.g., population of the highly excited cation followed by auto-ionization or direct population of the dication by the pump pulse). The KER spectra also display some time-dependent features that reflect the behavior of parts of the nuclear wave packet, as guided by the black solid lines. Those time-dependent features are symmetric about zero delay for both $\text{CH}_2^+ + \text{H}_2^+$ and $\text{CH}_3^+ + \text{H}^+$ channels. Interestingly, the time-dependent feature of the $\text{CH}_2^+ + \text{H}_2^+$ channel appears later than that of the $\text{CH}_3^+ + \text{H}^+$ channel for the positive delay. To show this phenomenon clearer, we take line-outs at the KER of 3.0 eV from Fig. 2a, b, which are shown in Fig. 2c. By fitting the time-dependent distributions, we find that the maximum of the time-dependent yields of the $\text{CH}_2^+ + \text{H}_2^+$ breakup channel appears ~ 20 fs later than that of the $\text{CH}_3^+ + \text{H}^+$ breakup channel at the KER of 3.0 eV. Fig. 2d shows the maxima of the time-dependent yields as a function of the KER for the two breakup channels. One can see that for all KERs the $\text{CH}_2^+ + \text{H}_2^+$ channel appears 20 ± 7 fs (within the 95% confidence interval) later than the $\text{CH}_3^+ + \text{H}^+$ channel.

To image the MD in real time, we further measured the three-body Coulomb explosion channel ($\text{CH}_2^+ + \text{H}^+ + \text{H}^+$), which could provide detailed information about the bond angles. In Fig. 3a, b, we show the Newton plots of the three-body breakup channel ($\text{CH}_2^+ + \text{H}^+ + \text{H}^+$) at different time delays.

For the three-body Coulomb explosion data in Fig. 3, we naturally classify the spot-like structures as S_1 , S_2 , and S_3 and map them to D_{2d} -like, C_{2v} -like, and C_{3v} -like configurations. Each configuration contributes to a range of momentum angular distribution decided by its initial bond lengths and angles. From the momentum distribution shown in Fig. 3, the S_2 spot-like structures correspond to C_{2v} symmetry configuration, S_3 is related to C_{3v} and D_{2d} , and S_1 is linking to all the three symmetry configurations. The portion of C_{2v} increases obviously from 8 to 28 fs,

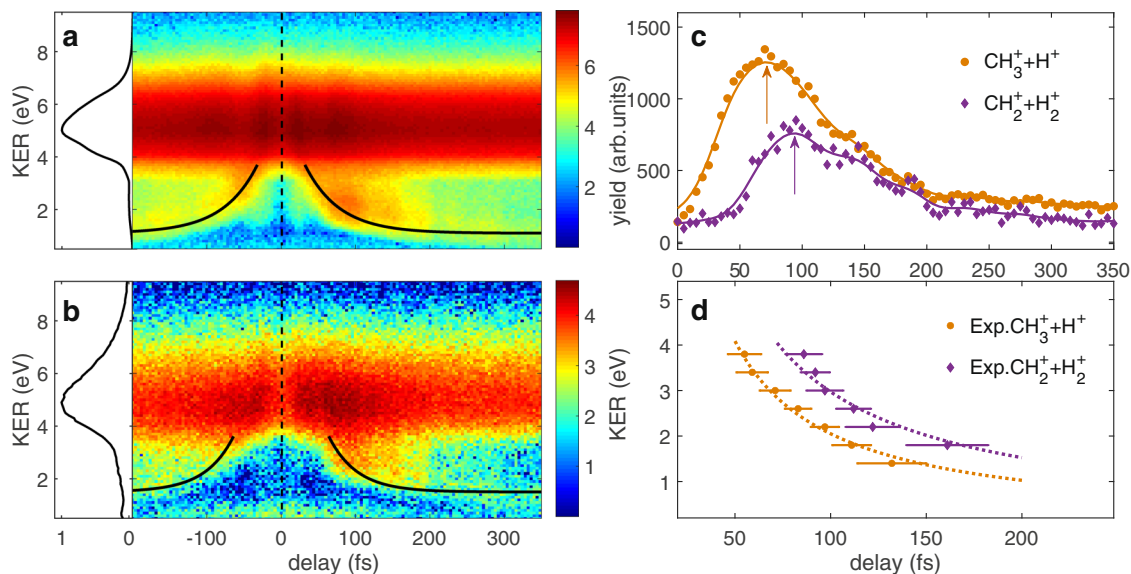


Fig. 2 Time evolution of two-body breakup channel. The measured ion yields with respect to the KER and the pump-probe time delay for the pathways of **a** $\text{CH}_3^+ + \text{H}^+$ and **b** $\text{CH}_2^+ + \text{H}_2^+$. The time-integrated KER distributions are shown in the left panels. The black solid curves in **a** and **b** are used to guide the time-dependent feature. **c** The measured ion yields with respect to the KER of 3.0 eV for the pathways of $\text{CH}_3^+ + \text{H}^+$ and $\text{CH}_2^+ + \text{H}_2^+$ (multiplied by a factor of 5 for visual convenience). The arrows show the peaks of the time-dependent distributions. **d** The peak extracted from the measured time-dependent distribution for different KERs. The dotted lines are the fits of the experimental data. The error bars represent the root-square deviation between the data and the fit used to extract the peak of the time-dependent distribution for each KER.

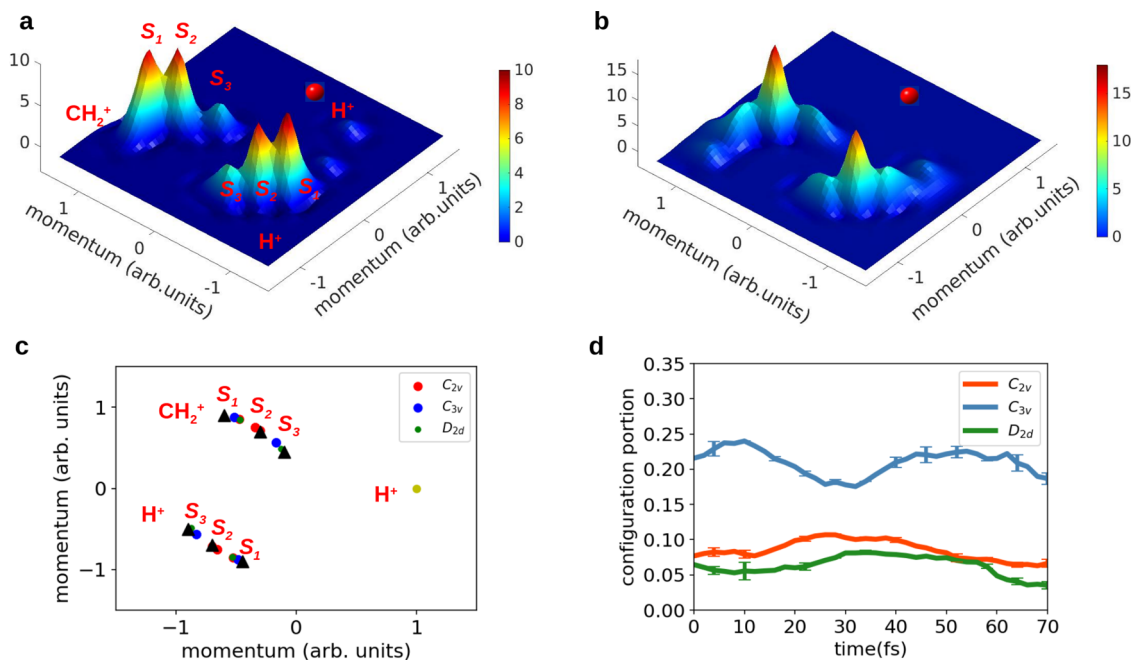


Fig. 3 Time evolution of three-body breakup channel. Newton plot of measurement result at the delay of **a** 8 fs and **b** 28 fs. Several spot-like structures in the Newton plot are indicated by S_1 , S_2 , and S_3 , which include contributions of molecular geometries of different symmetry types at the instant of Coulomb explosion. The momentum of one H^+ ion is set to be (1, 0). **c** Newton plot of C_{3v} , C_{2v} , D_{2d} configurations (see Supplementary Material). **d** The experimentally extracted evolution of C_{3v} -like, C_{2v} -like and D_{2d} -like geometries. The population of the C_{3v} and C_{2v} configurations peaks at 8 and 28 fs, respectively. The error bars represent the mean absolute deviation of the statistical errors.

which indicates the configuration evolution from C_{3v} to C_{2v} during the $\sim 20 \text{ fs}$ time delay coinciding with the two-body breakup channel in Fig. 2d.

Discussion

To interpret the experimental data, we employ MD method to simulate the CH_4^+ symmetry breaking and to understand the

unexpected long time delay of $\sim 20 \text{ fs}$ between the measured peak yields of $\text{CH}_3^+ + \text{H}^+$ and $\text{CH}_2^+ + \text{H}_2^+$ fragmentation channels.

Figure 4 illustrates how the simulated $\text{CH}_3^+ + \text{H}^+$ and $\text{CH}_2^+ + \text{H}_2^+$ yields peak at 10 and 25 fs, which is in qualitative agreement with the time difference from the two-body Coulomb explosion measurement. The peak time difference, which is essentially longer than the quarter of a period of any vibrational

mode, strongly implies complex dynamics involving multiple driving modes.

The peak time difference between the $\text{CH}_3^+ + \text{H}^+$ and $\text{CH}_2^+ + \text{H}_2^+$ channels of the two-body Coulomb explosion can be understood as follows. In the CH_4^+ cation, both f_2 bending mode and f_2 stretching mode lead to the C_{2v} structures of the lowest energy²¹. The f_2 bending mode enables relaxation from the 2F_2 state to the 2E state of C_{3v} configurations. The C_{3v} geometry of the CH_4^+ cation has one short and three long C–H bonds, which correlates with the $\text{CH}_3^+ + \text{H}^+$ breakup channel in the Coulomb explosion caused by the probe pulse (at the peak of the potential energy surface of Fig. 1). The C_{3v} geometry is the apex of the double cone with surrounding C_{2v} minima. In the C_{3v} geometry, the cation encounters again a doubly degenerate electronic state, which further relaxes to a lower symmetry via JT distortions²¹. Linear combination of symmetric modes, such as f_2 stretching and bending, subsequently leads the cation in C_{3v} geometry to land on the 2B_2 state of the lowest C_{2v} symmetry (at the bottom of the potential energy surface in Fig. 1). In the C_{2v} symmetric CH_4^+ , two long C–H bonds are separated by a small angle (53.3°) while two short C–H bonds are separated by a large angle (127.4°). The closest H–H distance in the C_{2v} geometry is 1.04 \AA ²¹, which is nearly the same as the equilibrium internuclear distance of H_2^+ (1.06 \AA). Similar to the neutral excited CH_4 molecule in the degenerate 1F_2 state²³, the deformation to C_{2v} via C_{3v} symmetric geometry in the 2B_2 cationic state finally provides the breakup channel $\text{CH}_2^+({}^1A_1) + \text{H}_2^+({}^2\Sigma_g^+)$ upon double ionization by the probe laser pulse. Thus the time difference between the $\text{CH}_3^+ + \text{H}^+$ and $\text{CH}_2^+ + \text{H}_2^+$ channels in Fig. 2 is equivalent to the characteristic time of the JT distortion from the C_{3v} to C_{2v} geometries of almost 20 fs.

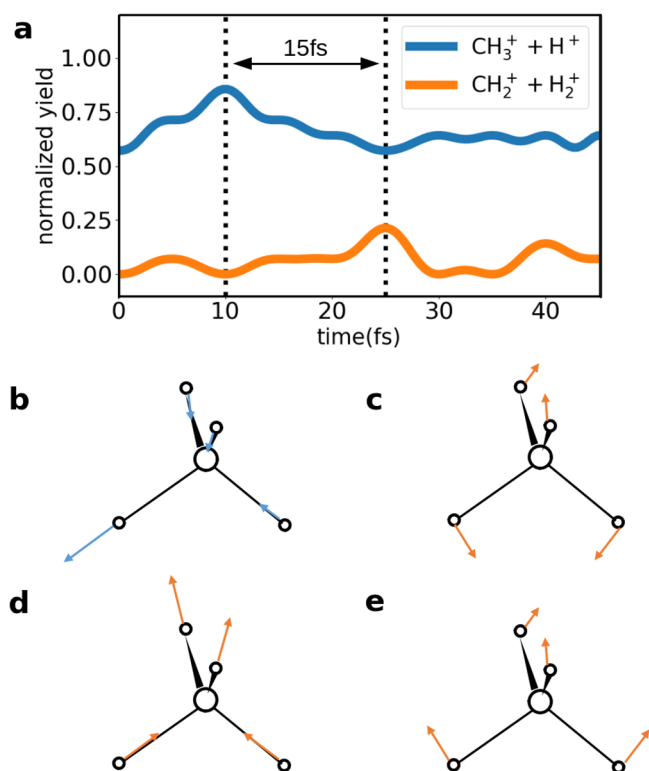


Fig. 4 Classical molecular dynamics simulation. **a** Normalized yield of each breakup channel of CH_4^+ trajectories. **b** f_2 stretching mode can lead to C_{3v} geometry and contribute to $\text{CH}_3^+ + \text{H}^+$ channel. **c** e bending mode, **d** f_2 stretching mode, and **e** f_2 bending mode can lead to D_{2d} or C_{2v} geometry and contribute to $\text{CH}_2^+ + \text{H}_2^+$ channel.

From Fig. 4b–e, the e bending mode results in D_{2d} geometry, while the f_2 mode leads to C_{3v} and C_{2v} geometry and the former is preferred²⁴. So the 10 fs peak for $\text{CH}_3^+ + \text{H}^+$ channel occurs when most CH_4^+ cations locate at C_{3v} geometry. Only the C_{3v} geometry from f_2 stretching mode will contribute to the $\text{CH}_3^+ + \text{H}^+$ channel, but both f_2 and e modes contribute to the $\text{CH}_2^+ + \text{H}_2^+$ channel. The three vibrations keep revival and dephasing periodically due to their commensurate frequencies, which result in the peak at 25 fs for the $\text{CH}_2^+ + \text{H}_2^+$ channel. This is because the revival brings constructive interference of the three vibrational modes (see Supplementary Material for detailed analysis). The ~ 15 fs time delay between the $\text{CH}_2^+ + \text{H}_2^+$ channel and the $\text{CH}_3^+ + \text{H}^+$ channel is in a good agreement with Fig. 3d. Combining the knowledge from the time-resolved two- and three-body measurements, the evolution of the molecular symmetry has been directly imaged. The excellent consistency of the results extracted from two- and three-body data confirms the accuracy and reliability of the direct imaging of CH_4^+ symmetry evolution.

The analysis from the ab initio classical MD can be refined with quantum wave packet dynamics simulation based on an effective Hamiltonian that maps the states involved in the $F \otimes (f \oplus e)$ JT effect of CH_4^+ onto the surface of a sphere^{12,25}. Each point represents a specific distorted geometry by e and f_2 bending mode, as shown in Fig. 5a. The center of each face corresponds to the C_{3v} structure, which has the highest potential energy, while the center of each line segment corresponds to the C_{2v} structure, which has the lowest potential energy. The time dependence of the population in the C_{2v} and D_{2d} configurations starting from a single C_{3v} configuration is presented in Fig. 5b calculated by the quantum wave packet dynamics simulation. One can see that the wave packet travels through an intermediate D_{2d} configuration, and the population of the C_{2v} configurations peaks at ~ 18.7 fs, which is consistent with the time difference of the $\text{CH}_3^+ + \text{H}^+$ and $\text{CH}_2^+ + \text{H}_2^+$ peaks in the two-body Coulomb explosion.

The theory uncovers more delicate structure beyond the precision limit of experimental observations, that there are two distinct local maxima at the instants of ~ 2.6 and ~ 18.7 fs in the time-dependent population of the C_{2v} geometry (Fig. 5b). To shed light on the origin of the two local maxima, we show in Fig. 5c the snapshots of wave packet density $\rho(t)$ of CH_4^+ cation starting from the C_{3v} geometry. At 2.6 fs, the nuclear wave packet delocalizes and part of the wave packet distorts to the C_{2v} geometries, which gives rise to the first local maximum in Fig. 5b. This time scale is consistent with previous studies using high-order harmonic spectroscopy^{18,26–28}. However, this is not the only pathway in the formation of the C_{2v} geometry for the methane cation. The nuclear wave packet can continue to spread on the surface of the sphere because the potential barriers between the C_{2v} minima are so low, the CH_4^+ wave packet can undergo a large amplitude motion^{10,13}. The nuclear wave packet forms a revival in the vicinity C_{2v} geometry at the back side of the sphere at 18.7 fs, which corresponds to the second local maximum in Fig. 5b. The interference fringes of the wave packet in Fig. 5c shows consistency with the physical picture of revival and dephasing dynamics.

In summary, we have directly measured the ultrafast structural dynamics and symmetry evolution during the onset of JT effect, and obtained the time during which the JT drives the CH_4^+ cation to deform from the higher symmetric C_{3v} down to the C_{2v} configurations, to be 20 ± 7 fs. We show that the nuclear wave packets of the methane cation experience complex multimode revival dynamics to reach the C_{2v} configurations. The interference among symmetric modes plays a significant role in the formation of the C_{2v} geometry during the JT distortion process. This has a broad impact on the understanding of the structural rearrangement triggered by strong laser pulses for the floppy molecular systems. Due to the universality of the JT effect, our study offers a possibility

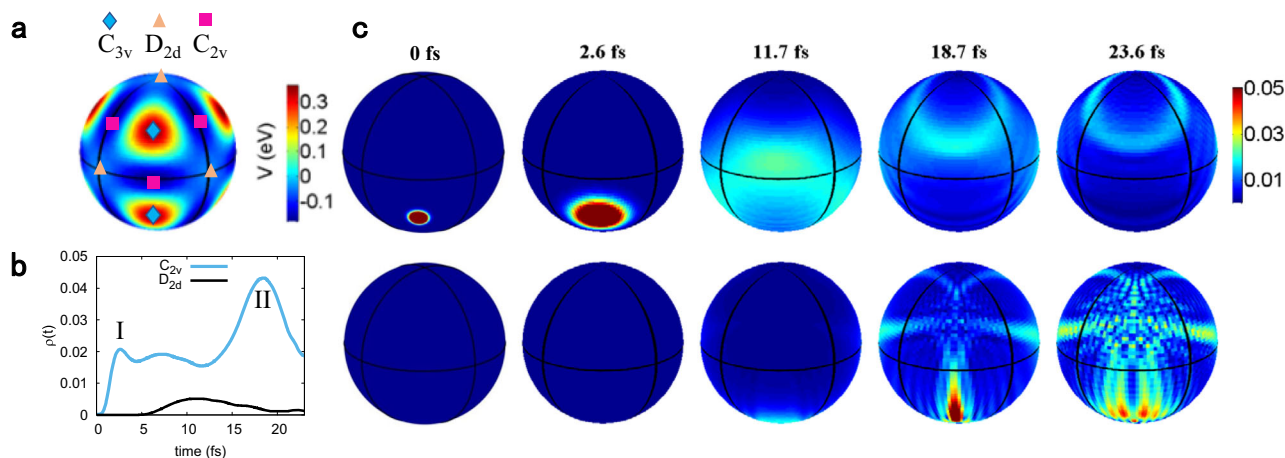


Fig. 5 Quantum wave packet dynamics simulation. **a** The potential energy surface of CH_4^+ cation in the sphere. **b** Time dependence of the populations in the C_{2v} and D_{2d} geometries of CH_4^+ cation. The results are obtained by initially putting the wave packet on the C_{3v} geometry. I and II represent two distinct local maxima for the populations in the C_{2v} geometry. **c** Snapshots of wave packet density $\rho(t)$ of CH_4^+ cation in the sphere starting from C_{3v} geometry. **c** Top and bottom rows correspond to the front and back views of the sphere, respectively.

to obtain experimental information of detailed structural features and intramolecular dynamics of the floppy molecules and reveals the symmetry breaking dynamics in ultrashort time scale.

Methods

Experimental methods. The experiment was performed using linearly polarized radiation from a Ti:sapphire laser system at 800-nm central wavelength with ~25 fs pulse width (full width at half maximum, FWHM). The laser pulse was split in a Mach-Zehnder type interferometer providing two nearly identical pulses separated by a time delay, which can be controlled by a motorized translation stage. The resulting two pulses were recombined before the vacuum chamber by using a beam combiner. The intensity of each laser pulse is estimated to be almost $3 \times 10^{14} \text{ W/cm}^2$. The laser beam was then focused into the vacuum chamber and interacted with the supersonic CH_4 molecules. We measured the three-dimensional momentum distributions of the ions using cold-target recoil-ion momentum spectroscopy²⁹.

Classical MD simulation. To simulate the experiment, a set of trajectories of the CH_4^+ cation is integrated up to 100 fs after the photo-ionization process. For each set of trajectories, CH_4^+ is promoted to CH_4^{2+} PES at selected time delays and the corresponding dissociation to either Coulomb explosion channel is determined by following the subsequent trajectory (see Supplementary Material).

Quantum wave packet dynamics simulation. To understand the dynamics of the JT distortion, we carried out wave packet dynamics simulation using the multi-configuration time-dependent Hartree method³⁰, based on an effective Hamiltonian by considering molecular symmetry. In the Hamiltonian, the potential of the corresponding $F \otimes (f \oplus e)$ JT effect of CH_4^+ is mapped onto the surface of a sphere^{12,25}, where the e and f_2 vibrational modes are parametrized by spherical harmonics of order $l=2$. The details of the simulation are explained in the Supplementary Material.

Data availability

The data that support the plots within this article is available from the corresponding authors upon reasonable request.

Code availability

The codes used for the molecular dynamics simulations are available from the corresponding author on reasonable request.

Received: 9 August 2020; Accepted: 14 June 2021;

Published online: 09 July 2021

References

- Jahn, H. A. & Teller, E. Stability of polyatomic molecules in degenerate electronic states - I - orbital degeneracy. *Proc. R. Soc. Lond. A* **161**, 220 (1937).

- Yang, J. et al. Imaging CF_3I conical intersection and photodissociation dynamics with ultrafast electron diffraction. *Science* **361**, 64–67 (2018).
- Higgs, P. W. Broken symmetries and the masses of gauge bosons. *Phys. Rev. Lett.* **13**, 508 (1964).
- von Busch, H. et al. Unambiguous proof for berry's phase in the sodium trimer: analysis of the transition $A^2E' \leftarrow X^2E'$. *Phys. Rev. Lett.* **81**, 4584–4587 (1998).
- Meiswinkel, R. & Köppel, H. A pseudo-Jahn-Teller treatment of the pseudorotational spectrum of Na_3 . *Chem. Phys.* **144**, 117–128 (1990).
- Ernst, W. E. & Rakowsky, S. Integer quantization of the pseudorotational motion in Na_3B . *Phys. Rev. Lett.* **74**, 58–61 (1995).
- Knight, L. B., Steadman, J., Feller, D. & Davidson, E. R. Experimental evidence for a C_{2v} (2B_1) ground-state structure of the methane cation radical: ESR and ab initio CI investigations of methane cation radicals (CH_4^+ and CH_4^+) in neon matrices at 4 K. *J. Am. Chem. Soc.* **106**, 3700–3701 (1984).
- Knight, L. B. et al. Electron spin resonance studies of the methane radical cations ($^{12,13}\text{CH}_4^+$, $^{12,13}\text{CDH}_4^+$, $^{12}\text{CD}_2\text{H}_4^+$, $^{12}\text{CD}_3\text{H}^+$, $^{12}\text{CD}_4^+$) in solid neon matrices between 2.5 and 11 K: analysis of tunneling. *J. Chem. Phys.* **103**, 3377–3385 (1995).
- Lindner, R., Müller-Dethlefs, K., Wedum, E., Haber, K. & Grant, E. R. On the shape of C_6H_6^+ . *Science* **271**, 1698–1702 (1996).
- Wörner, H. J., Qian, X. & Merkt, F. Jahn-Teller effect in tetrahedral symmetry: Large-amplitude tunneling motion and rovibronic structure of CH_4^+ and CH_4^+ . *J. Chem. Phys.* **126**, 144305 (2007).
- Wörner, H. J., Qian, X. & Merkt, F. Erratum: Jahn-Teller effect in tetrahedral symmetry: Large-amplitude tunneling motion and rovibronic structure of CH_4^+ and CH_4^+ . *J. Chem. Phys.* **154**, 069901 (2021).
- Jacovella, U., Wörner, H. J. & Merkt, F. Jahn-teller effect and large-amplitude motion in CH_4^+ studied by high-resolution photoelectron spectroscopy of CH_4 . *J. Mol. Struct.* **343**, 62–75 (2018).
- Wörner, H. J., van der Veen, R. & Merkt, F. Jahn-Teller effect in the methane cation: rovibronic structure and the geometric phase. *Phys. Rev. Lett.* **97**, 173003 (2006).
- Wörner, H. & Merkt, F. Jahn-Teller effects in molecular cations studied by photoelectron spectroscopy and group theory. *Angew. Chem. Int. Ed.* **48**, 6404–6424 (2009).
- Sen, S. & Mondal, T. The Jahn-Teller effect in the ground electronic state of the tetrafluoromethane cation before dissociation: a promoter of the anisotropic fragmentation. *Mol. Phys.* **117**, 2487–2499 (2019).
- Vager, Z. et al. Direct determination of the stereochemical structure of CH_4^+ . *Phys. Rev. Lett.* **57**, 2793–2795 (1986).
- Vager, Z., Graber, T., Kanter, E. P. & Zajfman, D. Direct observation of nuclear rearrangement in molecules. *Phys. Rev. Lett.* **70**, 3549–3552 (1993).
- Baker, S. et al. Probing proton dynamics in molecules on an attosecond time scale. *Science* **312**, 5 (2006).
- Schaniel, D., Nicoul, M. & Woike, T. Ultrafast reversible ligand isomerisation in $\text{Na}_2[\text{Fe}(\text{CN})_5\text{NO}]2\text{H}_2\text{O}$ single crystals. *Phys. Chem. Chem. Phys.* **12**, 9029–9033 (2010).
- Pertot, Y. et al. Time-resolved X-ray absorption spectroscopy with a water window high-harmonic source. *Science* **355**, 264–267 (2017).
- Frey, R. F. & Davidson, E. R. Potential energy surfaces of CH_4^+ . *J. Chem. Phys.* **88**, 1775–1785 (1988).

22. Bocharova, I. A. et al. Time-resolved Coulomb-explosion imaging of nuclear wave-packet dynamics induced in diatomic molecules by intense few-cycle laser pulses. *Phys. Rev. A* **83**, 013417 (2011).
23. Koseki, S., Shimakura, N., Teranishi, Y., Lin, S. H. & Fujimura, Y. Neutral fragmentation paths of methane induced by intense ultrashort IR laser pulses: Ab initio molecular orbital approach. *J. Phys. Chem. A* **117**, 333 (2013).
24. Bersuker, I.B. *The Jahn-Teller Effect* (Cambridge University Press, 2006).
25. Chancey, C., O'Brien, M. & O'Brien, M. *The Jahn-Teller Effect in C₆₀ and Other Icosahedral Complexes* (Princeton University Press, 1997).
26. Madsen, C. B., Abusamha, M. & Madsen, L. B. High-order harmonic generation from polyatomic molecules including nuclear motion and a nuclear modes analysis. *Phys. Rev. A* **81**, 043413 (2010).
27. Mondal, T. & Varandas, A. J. C. On extracting subfemtosecond data from femtosecond quantum dynamics calculations: the methane cation. *J. Chem. Theo. Comput.* **10**, 3606–3616 (2014).
28. Mondal, T. & Varandas, A. J. C. Structural evolution of the methane cation in subfemtosecond photodynamics. *J. Chem. Phys.* **143**, 014304 (2015).
29. Ullrich, J. et al. Recoil-ion and electron momentum spectroscopy: reaction-microscopes. *Struct. Bonding* **71**, 1463–1545 (2003).
30. Beck, M. H., Jäckle, A., Worth, G. A. & Meyer, H.-D. The multiconfiguration time-dependent Hartree method: a highly efficient algorithm for propagating wavepackets. *Phys. Rep.* **324**, 1–105 (2000).

Acknowledgements

This work is supported by National Key Research and Development Program of China (Grant no. 2019YFA0308300) and National Natural Science Foundation of China (Grant nos. 11722432, 12021004, 92050201, and 61475055). Z.L. and M.Z. are grateful to Yajiang Hao and Changjian Xie for helpful discussions.

Author contributions

M.L., M.Z. contributed equally to this work. M.L., K.G., Q.S., W.C., S.L., J.Q., Y.Z., Y.L., and P.L. designed the experiment and carried out the measurement. M.Z., O.V., Z.G., Q.Z., X.G., L.C., and Z.L. performed the classical and quantum molecular dynamics

simulations. M.L., M.Z., O.V., and Z.L. prepared the manuscript. All authors contributed to finalizing and approving the manuscript.

Competing interests

The authors declare no competing interests.

Additional information

Supplementary information The online version contains supplementary material available at <https://doi.org/10.1038/s41467-021-24309-z>.

Correspondence and requests for materials should be addressed to W.C., Y.L., Z.L. or P.L.

Peer review information *Nature Communications* thanks the anonymous reviewers for their contribution to the peer review of this work. Peer reviewer reports are available.

Reprints and permission information is available at <http://www.nature.com/reprints>

Publisher's note Springer Nature remains neutral with regard to jurisdictional claims in published maps and institutional affiliations.



Open Access This article is licensed under a Creative Commons Attribution 4.0 International License, which permits use, sharing, adaptation, distribution and reproduction in any medium or format, as long as you give appropriate credit to the original author(s) and the source, provide a link to the Creative Commons license, and indicate if changes were made. The images or other third party material in this article are included in the article's Creative Commons license, unless indicated otherwise in a credit line to the material. If material is not included in the article's Creative Commons license and your intended use is not permitted by statutory regulation or exceeds the permitted use, you will need to obtain permission directly from the copyright holder. To view a copy of this license, visit <http://creativecommons.org/licenses/by/4.0/>.

© The Author(s) 2021